Synthesis and emission dynamics of Sub-3 nm upconversion nanoparticles

B. Amouroux, A. Eftekhari, C. Roux, J. C. Micheau, P. Roblin, M. Pasturel, F. Gauffre, C. Wuerth, U. Resch-Genger, Michel Sliwa, et al.

RESEARCH ARTICLE

ADVANCED OPTICAL MATERIALS
www.advopticalmat.de

Synthesis and Emission Dynamics of Sub-3 nm Upconversion Nanoparticles

Baptiste Amouroux, Ali Eftekhari, Clément Roux, Jean-Claude Micheau, Pierre Roblin, Mathieu Pasturel, Fabienne Gauffre, Christian Würth, Ute Resch-Genger, Michel Sliwa, Aude Bouchet, and Christophe Coudret**

Reducing the size of upconversion nanoparticles (UCNPs) down to a few nm yields luminescent materials containing a very small number of emitters. Considering the bottom limit of one activator per particle ultrasmall UCNPs offer an unprecedented platform to study the contributions of the different energy transfers at play in upconversion luminescence. Maintaining detectable emission despite the limited number of emitting ions and the high surface-to-volume ratio requires suitable particle architectures. $Na(Gd-Yb)F_4:Tm^{3+}$ emissive sub-3 nm diameter β-phase UCNPs are prepared using a gadolinium-rich composition in situ mixing of the precursors and a microwave high-temperature cycling sequence allowing precise control of the particle size and dispersity. These cores are coated with a $NaGdF_4$ inert shell to minimize the deleterious influence of surface quenching (SQ). Time-resolved luminescence measurements combining standard NIR excitation of the Yb^{3+} sensitizer and direct UV excitation of the Tm^{3+} activator are performed to quantify cross relaxation and surface quenching processes. The fine tuning of the number of activators per particle via an optimized synthesis pathway along with the use of an appropriate excitation scheme enabled to provide an accurate analysis of the different mechanisms at play in these model nanoparticles and to characterize the structure of the core-shell architecture.

1. Introduction

Among all spectral shift processes upconversion (UC) (or anti-Stokes shift) i.e. the ability of a material to convert low-energy photons into higher-energy photons is one of the most fascinating ones. A well-studied family of upconversion materials is lanthanide (Ln)-based upconversion phosphors. The remarkable spectroscopic behavior of these elements i.e. a regular energy spacing of long-lived excited states enables multiple-photon absorption at excitation powers lower than those required for classical two-photon absorption. The energy accumulated by the so-called "activator" aka "excited state absorption" ESA or "photon addition" results in the emission of shorter-wavelength photons.[1] The intrinsic low absorption cross-section of the Ln elements due to symmetry-forbidden f-f transitions[2] can be partly compensated by the addition of a sensitizer such as ytterbium ions Yb^{3+}. The most characteristic feature of Ln-UCNPs is that

B. Amouroux, C. Roux, J.-C. Micheau, C. Coudret
SOFTMAT Université de Toulouse CNRS UMR 5623
Université Paul Sabatier 118 route de Narbonne
Cedex 9, Toulouse 31062, France
E-mail: christophe.coudret1@univ-tlse3.fr

B. Amouroux
Laboratory for Vascular Translational Science LVTS INSERM UMR 1148
Université Sorbonne Paris Nord Université Paris Cité
Bobigny F93017, France

A. Eftekhari, M. Sliwa, A. Bouchet
Univ. Lille CNRS UMR 8516 LASIRE Laboratoire de Spectroscopie pour les Interactions
la Réactivité et l'Environnement
Lille F59 000, France
E-mail: aude.bouchet@univ-lille.fr

A. Eftekhari
Faculty of Engineering & Natural Sciences
Tampere University
P.O. Box 541, Tampere 33101, Finland

P. Roblin
Laboratoire de Génie Chimique
Fédération Fermat INPT CNRS Université de Toulouse
Toulouse 31062, France

M. Pasturel, F. Gauffre
Univ Rennes CNRS ISCR-UMR6226
Rennes F-35000, France

C. Würth, U. Resch-Genger
Bundesanstalt für Materialforschung und-prüfung (BAM) Department 1
Division Biophotonics
Richard Willstätter Straße 11
12489 Berlin, Germany

The ORCID identification number(s) for the author(s) of this article can be found under https://doi.org/10.1002/adom.202303283

DOI: 10.1002/adom.202303283

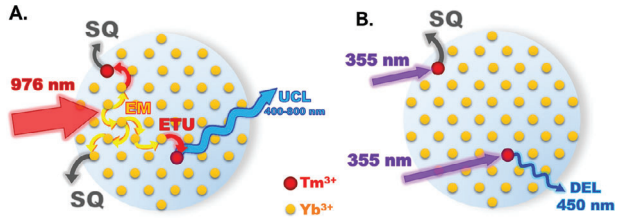

Scheme 1. Characteristic energy transfer processes encountered within ultrasmall UCNPs A) upon NIR irradiation of the sensitizers driving upconverted luminescence (UCL) or B) upon direct UV irradiation of the activator driving direct excitation luminescence (DEL). Decreasing the size of UCNPs to less than 3 nm results in an increase in surface quenching and a decrease of the number of Tm^{3+} ions per particle reducing the probability of cross-relaxation.

numerous processes are at work to redistribute the energy within the crystal (**Scheme 1**). Sensitizer-to-activator energy transfer upconversion (ETU) cross relaxation (CR) between two activators energy migration (EM) between sensitizers and sensitizer and activator radiative and nonradiative relaxations are among the main energy redistribution processes[3,4] with the latter occurring through matrix phonons. Moreover coupling with molecular vibrations from ligands bound on the crystal surface gives rise to surface quenching (SQ). These numerous interleaved processes explain the intrinsic highly nonlinear response of the emissions to the excitation power and the difficulty in quantifying each energy path following NIR irradiation. The complexity of such a dynamic network makes it difficult to predict the UCNP efficiency under stationary NIR irradiation[5,6] which is useful for the design of novel photonic devices or innovative biological imaging probes.[7–9]

Extremely small nanoparticles (less than 10 nm) are the subject of intense research as their size is close to that of biomolecules so they can easily match subcellular structures without disturbing cellular functions and they can be readily cleared by a living animal.[10–12] However such small objects contain a low amount of atoms and a large proportion is consequently close to or lie on the surface leading to a very strong surface quenching and a low luminescence.[13–15]

On the other hand molecular heteronuclear complexes composed of a handful of Ln ions with a defined arrangement between sensitizers and activators can display upconversion phenomenon.[16–20] This suggests that the bottom limit for observing upconversion in NPs is when only a single activator remains in the crystal. For the classical Tm^{3+} content of 1%[21] a single activator-UCNP has to comprise 100 rare earth (RE) atoms which corresponds to a diameter smaller than 2.5 nm for a typical $NaREF_4$ unit cell volume of 0.11 nm^3. An increase in diameter from 2.5 nm to 3 nm for UCNPs containing 1% Tm^{3+} will result in a change from one to two activators per UCNP on average. Such a size is also noticeably close to the recently described giant molecular clusters.[22,23]

M. Sliwa
LOB, CNRS, INSERM, École Polytechnique
Institut Polytechnique de Paris
Palaiseau 91120, France

The goal of the present work is to control the crucial synthesis parameters to obtain ultrasmall (US) UCNPs with a single activator. While very efficient preparations of 10 to 40 nm UCNPs are now available[24] little is known about ultrasmall-size UCNPs (< 10 nm)[25–32] and even less is known about UCNPs with sizes smaller than 3 nm. Obstacles to UCNP size reduction are first the difficult control of the host matrix crystallinity during synthesis. $NaREF_4$ exists in two polymorphs the kinetic α-polymorph and the thermodynamic β-polymorph. The hexagonal β-phase is particularly attractive: first it tolerates RE blends over a large range of proportions.[33] Second its low phonon energy which limits energy relaxation via crystal vibrations and the noncentrosymmetric local environment around the RE ions are favorable for activator radiative decay.[34–36] The synthetic challenge is thus to carefully control the reaction conditions not only to prepare particles of the pure β-polymorph with such a small mean diameter but also to ensure a narrow particle size distribution (PSD). To comply with this complex situation "burst nucleation" kinetic models predicting the PSD of ultrasmall nanocrystals made of a single polymorph had to be adapted.[37,38] As shown by the Haase group the narrowest β-phase PSD should be found immediately after the unstable α-polymorph has vanished by feeding the growing β-polymorph.[39] The second obstacle is obtaining ultrasmall emissive UCNPs since SQ caused by surface defects and surface-bound molecules becomes prominent for very small crystals.[15,40,41] Strategies to improve the emission of nanoparticles include firstly the increase of the concentration of Yb^{3+} sensitizer. A larger amount of Yb^{3+} ions per particles rises the 980 nm cross-section which in turn increases the chances of Yb-to-Tm energy transfer. However the drawback is that fast EM processes then channel the collected energy to the surface. Thus the second strategy is to limit energy leaking at the surface by depositing an insulating shell.[13,42–44]

Here we report an original synthetic strategy inspired by temperature cycling: the application of sharp temperature changes during crystallization.[45] The warming up of a suspension of microcrystals induces dissolution of the smallest microcrystals while subsequent cooling allows the surviving microcrystals to grow from the supersaturated solution (Ostwald ripening). Temperature cycling is used to control e.g. the size and size distribution of micro- to macrocrystals of proteins or pharmaceutical compounds[46–48] yet such a crystallization technique is scarcely used for the preparation of nanocrystals.[49] Only a single related approach has been recently utilized for the preparation of UCNPs by Li et al.[50] The authors with a different intention to that presented in this work sought to decouple nucleation and growth i.e. to ensure that no new nucleation could happen during the ripening steps using a specific structured heating process based on two steps (cycles + high temperature plateau) with a standard heating mantle. We have previously explored the MW-preparation of $Na(Gd_{0.42}\text{-}Yb_{0.57})F_4{:}Tm^{3+}_{0.01}$ UCNPs[51] for which the use of gadolinium promotes abundant β-phase nucleation as well as the formation of sub-10 nm nanocrystals over a large range of Gd:RE ratios.[52–55] Furthermore we have shown that a separate and slow introduction of sodium and fluoride sources into the cold rare-earth oleate ($RE(OA)_3$) combined with the use of fast dielectric heating (microwave oven) yielded sub-5 nm nanoparticles. The transformation was complete in 30 minutes at 300 °C. From these promising observations we improved

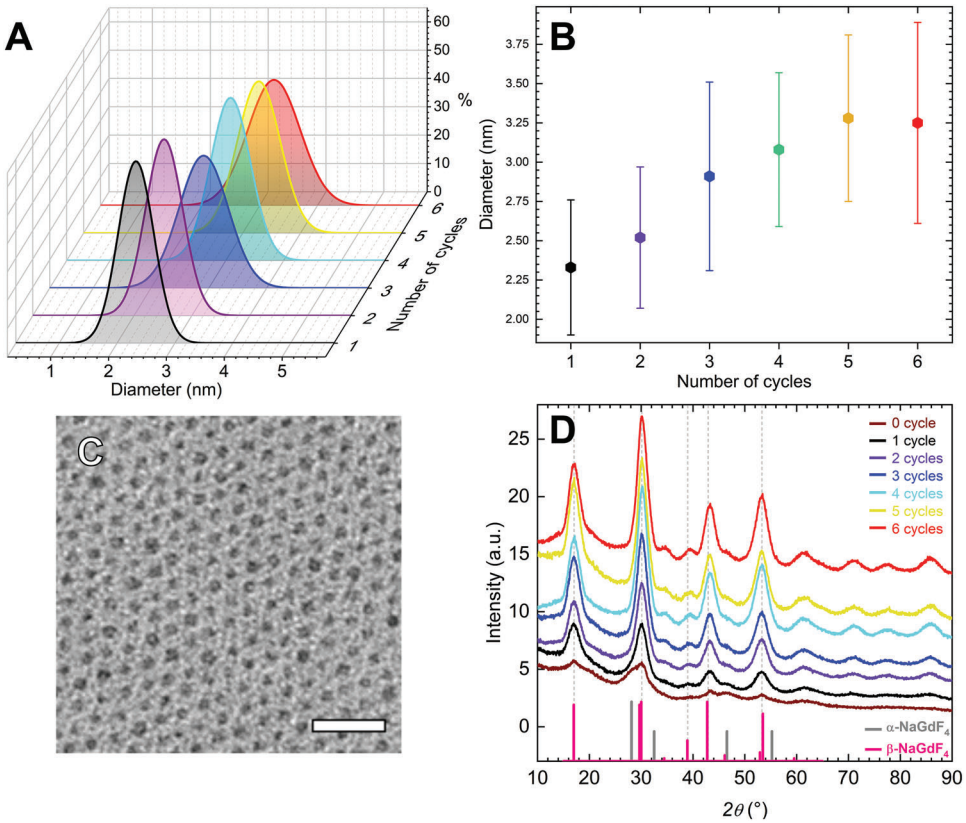

Figure 1. A) Evolution of the PSD obtained from TEM analysis and B) average diameter along with the standard deviation with the number of heating sequence cycles. C) Electron micrograph of the 6-cycle nanoparticles. The scale bar is 20 nm. D) XRD patterns of the particles prepared with 0 to 6 microwave-heating cycles along with XRD patterns of pure cubic (α) and hexagonal (β) $NaGdF_4$ crystals.

our protocol by using the MW-temperature cycling allowing the elimination of all other transient inorganic phases (α-$NaREF_4$ polymorph or NaF)[56] while controlling the particle average diameter and PSD.

In this work we show that by using temperature cycling during high-temperature precipitation it is possible to prepare highly monodisperse homogeneous Gd-rich β-phase UCNPs of less than 2.5 nm diameter with a limited number of Tm emitting ions and with a variable Yb content. Emission decay analysis during the temperature cycling was found to provide a precise description of the extent of β-phase crystallization in these nanometric

The photophysics of these ultra small nanoparticles containing a low amount of Tm^{3+} ions was further investigated. Taking into account that Tm^{3+} ions are statistically distributed among the particles as recently stressed out by Van Veggel et al. for 20 nm-nanocrystals prepared to contain only one activator[57] we have examined the dynamics of the energy redistribution among the few Tm^{3+} ions. The kinetic network is expected to be greatly simplified in this case thanks to a limited probability of CR (CR will be null for one single activator). The impact of sensitizer and activator concentrations on the upconversion emission dynamics was examined by evaluating the emission lifetimes under ns 976 nm excitation. Furthermore ns direct UV excitation of the Tm activator at 355 nm also provided useful information about the kinetic rate constants of highly excited Tm levels independent of the ETU and EM processes[58] and allowed us to address the structure of the shell in core-shell architectures.

2. Results and Discussion

2.1. Toward the Synthesis of Sub-3 nm UCNPs

A first set of experiments was carried out to combine the conditions and the original composition we previously explored[51] with those proposed by Li et al.[50] A critical step was to determine the optimal heating sequence (length and number of heating cycles). Careful monitoring of the broadening of the PSD by TEM allowed us to follow the progress of the transformation and determine the best growth conditions (**Figure 1**A–C; Figure S1, Supporting Information). The most promising minimal temperature cycle consisted of a 1-minute plateau at 300 °C (T_{high}) and a 5-minute plateau at 280 °C (T_{low}) using a monomode microwave oven allowing to program sharp changes in temperature (cooling in 2 s and heating in 1 min in this temperature range). The additional 30 min high-temperature plateau suggested by Li et al.[50] was unnecessary in the present case. In accordance with the apparatus limitations (maximum of 30 min for the entire sequence in the range 280–300 °C) a temperature sequence composed of a number of cycles varying from 1 to 6 was then applied. While the PSD was found to remain extremely narrow ($\sigma < 0.65$) the evolution of the average size with the number of cycles was found

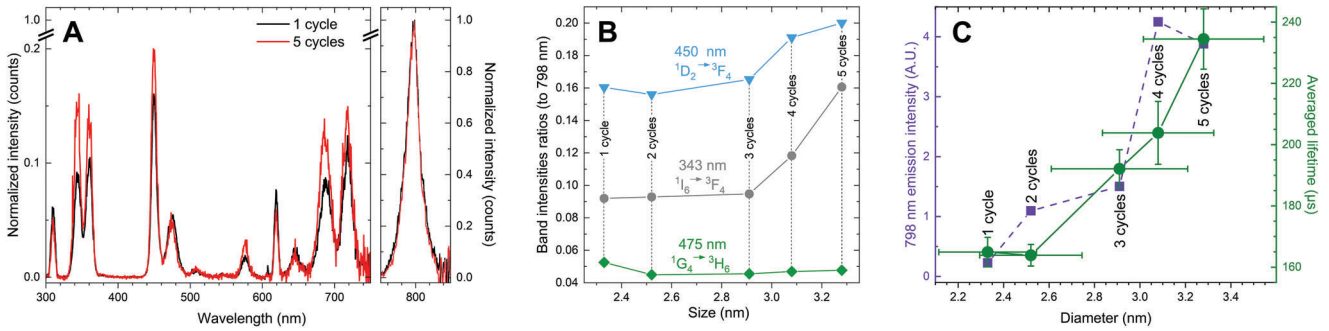

Figure 2. A) Steady-state UC luminescence spectra of the particles prepared after 1 and 5 microwave heating cycles. Intensities are normalized to the 798 nm emission. B) Band intensity ratios extracted from steady-state spectra of the particles prepared after 1 to 5 microwave heating cycles at 343 nm (grey) 450 nm (blue) and 474 nm (green). C) Steady-state luminescence intensity at 798 nm of the particles prepared after 1 to 5 microwave heating cycles (purple left vertical axis). Average lifetimes calculated from the amplitude-weighted sum of the time constants obtained from biexponential fitting of the decay at 798 nm (green right vertical axis).

to be limited. TEM analyses (Figure 1B) showed that the average diameter obtained was always smaller (between 2 and 3.5 nm) than that for our original protocol (4.6 nm)[51] demonstrating the impact of temperature cycling. Therefore other criteria besides the morphological one had to be checked to select the optimal number of cycles.

For this purpose the crystallinity of the particles was monitored by XRD measurements. The data was analyzed by deconvolving the diffractograms using TOPAS software (Bruker) in order to access the respective proportions of the α and β phases for the successive heating steps (Figure 1D, Table S1, Supporting Information). A poorly crystalline β-phase coexisting with the α-phase was identified in the reaction mixture before the heating cycles (see 2θ = 28 and 30°). After the first cycle the hexagonal β-polymorph was detected as the main component present along with a detectable amount of NaF. This composition rapidly evolved as the synthesis progressed and the analyzed particles were found to be composed of solely (within the detection limit of the technique) the β-phase from the 3rd cycle. The subsequent ripening thus implied only one polymorph. The unexpectedly high amount of β-phase at the very early stages of synthesis in the mixture can be related to the reported room-temperature preparation of $NaGdF_4$:$Eu^{3+}$$Er^{3+}$ β-phase nanocrystallites achieved by stirring a mixture of NaCl $RE(OAc)_3$ and NH_4F in anhydrous ethylene glycol for 25 h.[59]

An investigation of the emission properties of particles prepared with 1 to 5 microwave-heating cycles was performed to provide more thorough information on the α-to-β phase transition. Steady-state luminescence spectra were monitored for the 5 types of particles (1 to 5 microwave heating cycles) upon CW 976 nm irradiation (**Figure 2**). The evolution of the luminescence intensity at 798 nm (Figure 2C purple square dots) is characterized by a weak luminescence observed for particles prepared with one heating cycle. This is consistent with the small size of the particles expected to be heavily quenched due to a large surface-to-volume ratio[14] and the existence of the poorly luminescent α-phase.[60] A noticeable increase in the emission intensity is observed with increasing number of cycles. It then remains roughly constant after 4 to 5 cycles. A detailed analysis of the steady-state spectra in Figure 2A shows that the relative intensities of the Tm^{3+} emission bands (normalized by the emission at 798 nm) arising from the high-energy states (343 360 450 and 576 nm) are almost constant for the 1- to 3-cycle particles before increasing for particles obtained after 4 and 5 cycles (Figure 2B; Figure S2, Supporting Information). The increase in the contribution of the UV-emission bands to the steady-state spectrum is assigned to the α-to-β phase conversion as previously reported for Na(Y-Yb)F_4:Tm^{3+} microcrystals.[61] This is in agreement with the XRD results.

In addition analysis of the upconversion emission decay time constants also provides a relevant descriptor of the α-to-β phase transition during the temperature sequence. Here a square pulse of 3 milliseconds enables photostationary emission of the 798 nm emission of Tm^{3+}. The luminescence decay at 798 nm of the particles obtained after 1 to 5 microwave-heating cycles is shown in Figure S3 (Supporting Information). Emission amplitude-averaged lifetimes were calculated from the biexponential fit of the decay curve. The analysis of these effective lifetimes as a function of the number of heating cycles (Figure 2C green round dots) clearly shows a jump after cycle 2. The average lifetime ranges from 165 µs for 1 cycle to approximately 235 µs ± 10 µs for 5 cycles (Table S3, Supporting Information). After 2 cycles the average lifetime increases almost linearly with size. This indicates that completion of the α-to-β phase transition is already achieved from the third heating cycle. After that stage the particle has reached a fully β-crystal phase and the lengthening of the lifetime with increasing size of UC-NPs is due to the decrease in the surface-to-volume ratio (for a sphere 6/d) and thus to the decrease in surface quenching.

To confirm the necessity of the high-temperature cycling sequence using dielectric heating the standardized conventional heating procedure[24] was also used. With this method 20% Yb^{3+} sub-10 nm Na(Gd-Yb)F_4:Tm^{3+} UCNPs were also obtained but with a larger diameter (7.3 nm Figure S4A, Supporting Information). Therefore thermal cycling induces a change in the PSD due to the fast dissolution of the very small particles (heating-up steps) and fast growth of the remaining particles (cooling-down steps). This result is in accordance with De Groot et al. suggestions for larger crystals.[62] The duration of each plateau is important to allow PSD relaxation via Ostwald ripening and moderate the increase in the average size. It is likely that these conditions are achieved for the ultrasmall particles described here which

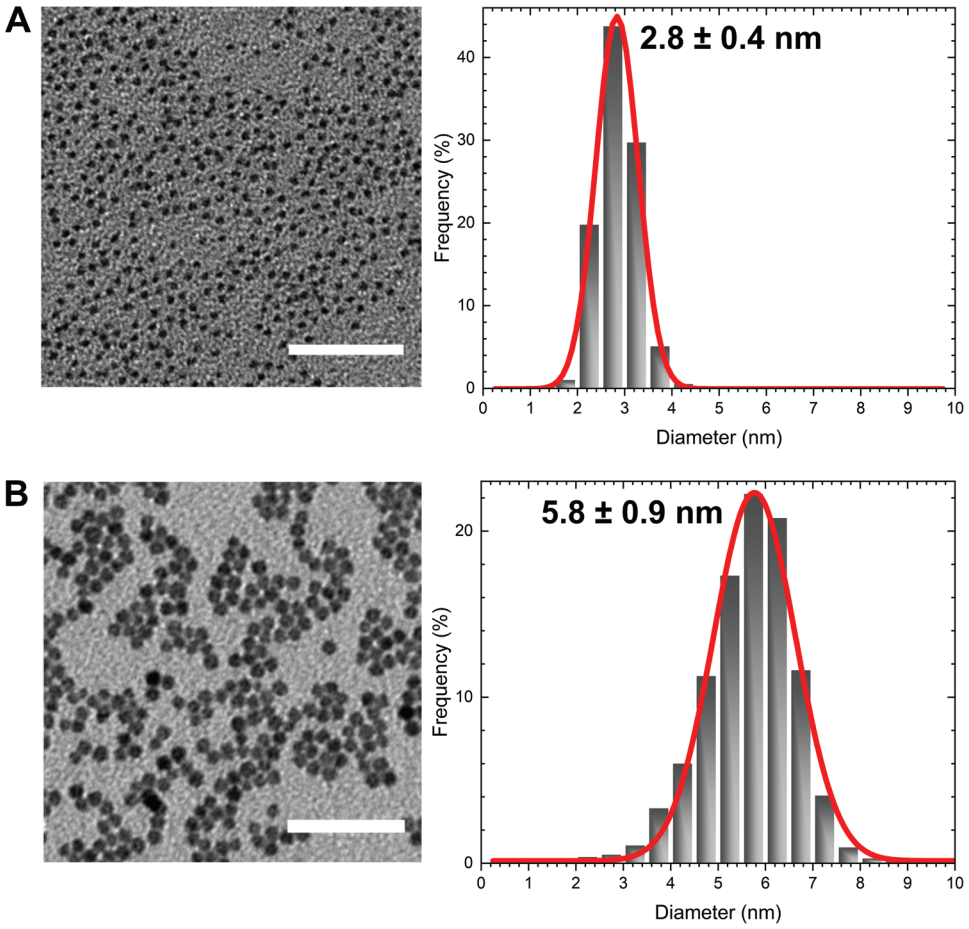

Figure 3. TEM images and PSD of 57%Yb^{3+} 1%Tm^{3+} UCNPs prepared with 5 heating cycles (A: core, B: core-shell, scale bar = 50 nm).

could explain the apparent slow increase in NP size during the first 6 cycles.

As it has been reported that substantial variability in the average UCNP diameter could be observed for a defined synthetic protocol[63,64] the abovementioned synthesis of $Na(Gd_{0.42}Yb_{0.57})F_4:Tm^{3+}_{0.01}$ was repeated several times. Ultrasmall UCNPs could be again prepared ranging from 3.9 nm down to 2.8 nm in diameter with a constant PSD owing to the heating cycle method. The target size for single-Tm-ion UCNPs (2.8 nm diameter) was finally reached (**Figure 3**A). Ultrasmall UCNPs of similar sizes (2.4 nm diameter) were also obtained using the more conventional 20% Yb^{3+} formulation (Figure S4B, Supporting Information). These two ultrasmall UCNPs batches were analyzed with ICP–OES which confirmed an average number of activator ions per particle of 1.2 and 1.8 Tm ions/NP with 23% and 58% Yb^{3+} compositions respectively.

An ideal "one-emitter particle" doped with 1% Tm would contain 100 RE atoms. Therefore their repartition can be modelled by a Poisson distribution law. Such a hypothesis has been experimentally controlled by Van Veggel et al.[57] In this case according to Poisson statistics one should find 37% (1/e) "empty" particles (activator free) 37% one-activator particles 18% ($1/e^2$) two-activator particles etc. Experimentally as the suitably binned PSD gives the frequencies of sizes $\{f_i\}$ the probability of finding one Tm^{3+} ion for a given size must be weighted by its frequency (Equation 1):

$$P\,(Tm = k) \;=\; \sum_{i\,=\,0}^{\infty} f_i \,\frac{1}{k!}\,(N_i)^k e^{-N_i} \qquad (1)$$

where f_i is the binned PSD frequency N_i is the ideal Tm^{3+} ion number per particle and k is the real Tm^{3+} ion number for which the probability P is calculated. **Figures** 4A and S5 (Supporting Information) indicate that the Tm^{3+} distributions per particle for the ultrasmall particles of the batches (Core 23% and 58% Yb) are almost identical (27% of UCNPs contain 1 Tm^{3+} ion) a value near the theory (37%). These batches are then labeled $NP^{23\%}_{2.4}$ and $NP^{58\%}_{2.8}$ (NP^{Y}_{X} X for the diameter of the particle in nm and Y the proportion of Yb^{3+} sensitizer see **Table** 1).

Core-shell nanoparticles were prepared by growing a shell of $NaGdF_4$ onto the previously prepared cores containing 23% Yb^{3+} (2.4 nm) and 58% Yb^{3+} (2.8 nm) using a protocol described by Zhai et al.[65] This procedure led in both cases to monodisperse particles of 5.8 ± 0.9 nm in diameter (Figure 3B; Figure S4B, Supporting Information). Powder XRD validates the β-phase nature of the NP material and the crystallite size (Figure 4C). The larger core-shell UCNPs consistently reveal narrower peaks (i.e 1.6° for

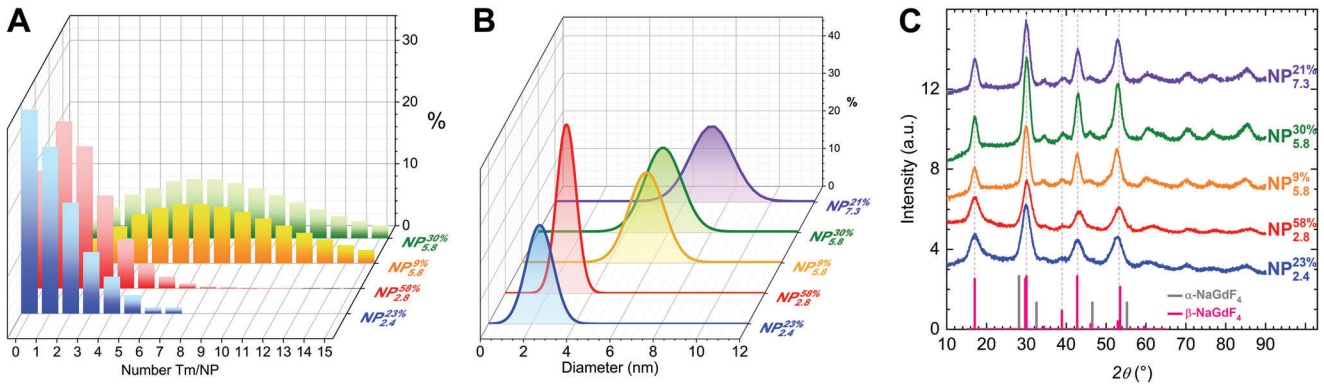

Figure 4. A) Tm^{3+} Poisson distributions B) PSD and C) XRD patterns of the UCNPs whose composition is given in Table 1.

$NP_{2.4}^{23\%}$ at $2\theta = 43°$) than the ultrasmall core nanoparticles (i.e 2.9° for $NP_{2.4}^{23\%}$ at $2\theta = 43°$) indicating a more extended crystal. ICP-OES analyses also confirm that the final Yb/Gd and Tm/Gd is close to the expected values according to the stoichiometry used (RE_{core}:Gd_{shell} 1:1). Final CS particles should then have only doubled their average volume which would have yielded core-shell particles of 3 to 3.5 nm in diameter. However the obtained particles are clearly larger and the resulting number of RE ions calculated from ICP and TEM analyses is also larger than expected (Table 1). This contrasts with the formation of a regular core-shell architecture directly from the parent $NP_{2.4}^{23\%}$ and $NP_{2.8}^{58\%}$ core particles. We hypothesize that CS-type NPs lie between two limit scenarios: (i) complete core dissolution followed by crystallization of cores and shell material leading to particles with a homogeneous repartition of all the RE atoms throughout the crystal and (ii) deposition of a shell onto sintered core particles thus leading to a "core-shell" architecture. The Poisson statistics applied for $NP_{5.8}^{9\%}$ and $NP_{5.8}^{30\%}$ (Figure 4A; Figure S5, Supporting Information) show that the number of Tm ions/NP should be considered similar (7 to 8) for the two CS NPs in the following.

2.2. Upconversion Emission Dynamics of Ultrasmall Nanoparticles

To unravel the emission dynamics of the prepared ultrasmall UCNPs different irradiation and excitation schemes were employed. This allows us to deconvolute the different parameters that control upconversion emission i.e. energy migration (EM) and ETU from Yb CR between Tm^{3+} ions and SQ (**Figure 5**). First UCNPs were investigated under steady-state conditions using CW 976 nm irradiation. Emission spectra between 300 and 850 nm are shown in **Figure 6** (normalized with respect to the 798 nm band). Despite their small size and limited number of emitters all particles displayed the usual Tm^{3+} emission bands between 345 and 800 nm. The contributions of the different emission bands to the total integrated emission signal (Figure 6C; Figure S6, Supporting Information) allow us to qualitatively address the effect of the modification of the NP architecture i.e. the number of Tm^{3+} versus Yb^{3+} ions and the existence of a shell.

The contribution of the 450 nm ($^1D_2 \rightarrow {}^3F_4$ 4 ETU) emission band to the total emitted signal (integrated from 300 to 850 nm) is higher for $NP_{2.4}^{23\%}$ $NP_{2.8}^{58\%}$ and NP core particles than for those designed as core-shell (CS) i.e. $NP_{5.8}^{30\%}$ and $NP_{5.8}^{9\%}$ (Figure 6C; Figure S6, Supporting Information). A possible explanation could be the involvement of some deleterious cross relaxation processes (CR4 Figure 5) between a ground state Tm^{3+} ion and a $^1D_2$ excited Tm^{3+} ion whose probability rises as the Tm^{3+} ion number increases as in $NP_{5.8}^{30\%}$ and $NP_{5.8}^{9\%}$. In the case of the larger $NP_{7.3}^{21\%}$ core particles the higher number of excited Tm^{3+} ions favors the possibility of having two excited Tm^{3+} ions concomitantly and thus the existence of CR1-3 processes that promote the $^1D_2$ state population. On the other hand a decrease in the Yb^{3+} content from 57%

Table 1. Composition size parameters and average numbers of Yb^{3+} and Tm^{3+} ions per NP in core and core-shell particles. $NP_{7.3}^{21\%}$ was obtained using a standardized conventional heating procedure.

Target Yb composition [%]	Core 20%	Core 57%	Core-shell 20%	Core-shell 57%	Core 20%
Diameter {nm}	2.4	2.8	5.8	5.8	7.3
ICP composition					
%Gd	75.5%	40.6%	90.4%	69.8%	77.5%
%Yb	23.1%	58.3%	9.0%	29.6%	21.2%
%Tm	1.35%	1.11%	0.60%	0.55%	1.29%
Notation	$NP_{2.4}^{23\%}$	$NP_{2.8}^{58\%}$	$NP_{5.8}^{9\%}$	$NP_{5.8}^{30\%}$	$NP_{7.3}^{21\%}$
S/V {nm^{-1}}	2.55	2.12	1.04	1.04	0.83
Average number Yb/NP[a)]	21	95	120	398	565
Average number Tm/NP[a)]	1.2	1.8	8.0	7.4	34.4

[a)] Average number of atoms/NP determined from the size measured by TEM and unit cell parameters obtained from XRD.

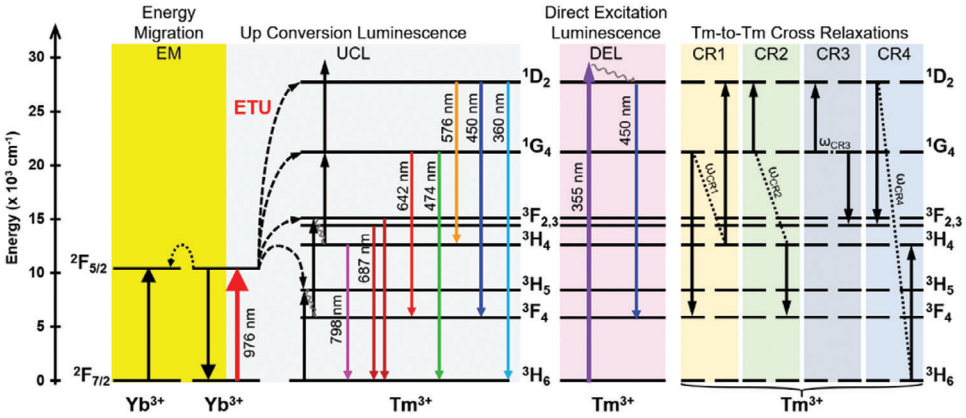

Figure 5. Energy level diagram of Yb^{3+}/Tm^{3+}-doped UCNPs highlighting the transitions explored upon 976 nm or 355 nm excitation and the four possible Tm-Tm CR processes (CR1 to CR4) involving the $^1D_2$ Tm^{3+} excited state.

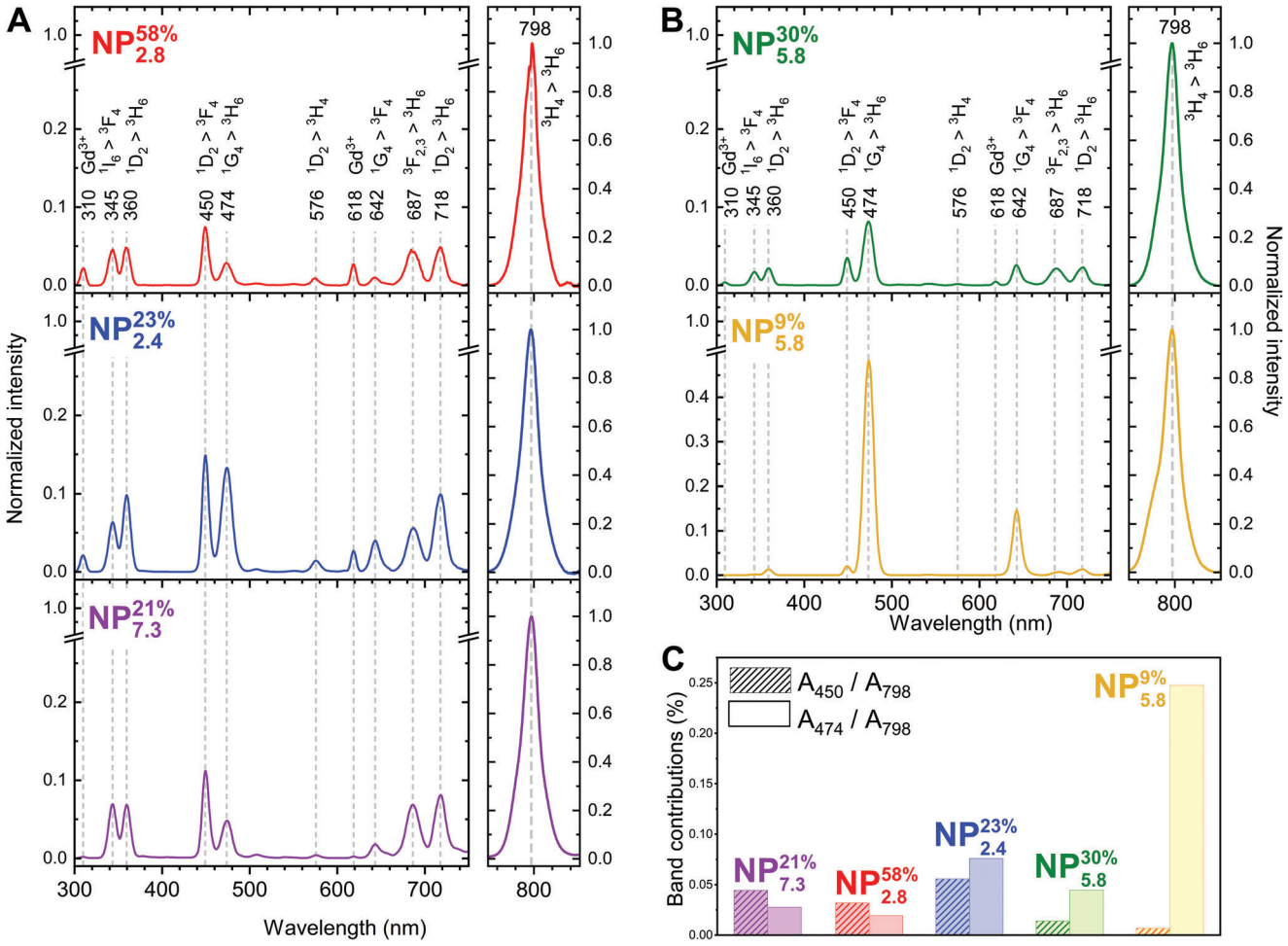

Figure 6. Steady-state spectra of core A) and core-shell B) particles upon CW 976 nm irradiation (6.85 kW cm^{-2}). Intensities are normalized with respect to the 798 nm band. C) Contributions of $^1D_2 \rightarrow {}^3F_4$ (450 nm) and $^1G_4 \rightarrow {}^3H_6$ (474 nm) bands to the total emission signal (integrated from 300 to 850 nm) for the different nanoparticles.

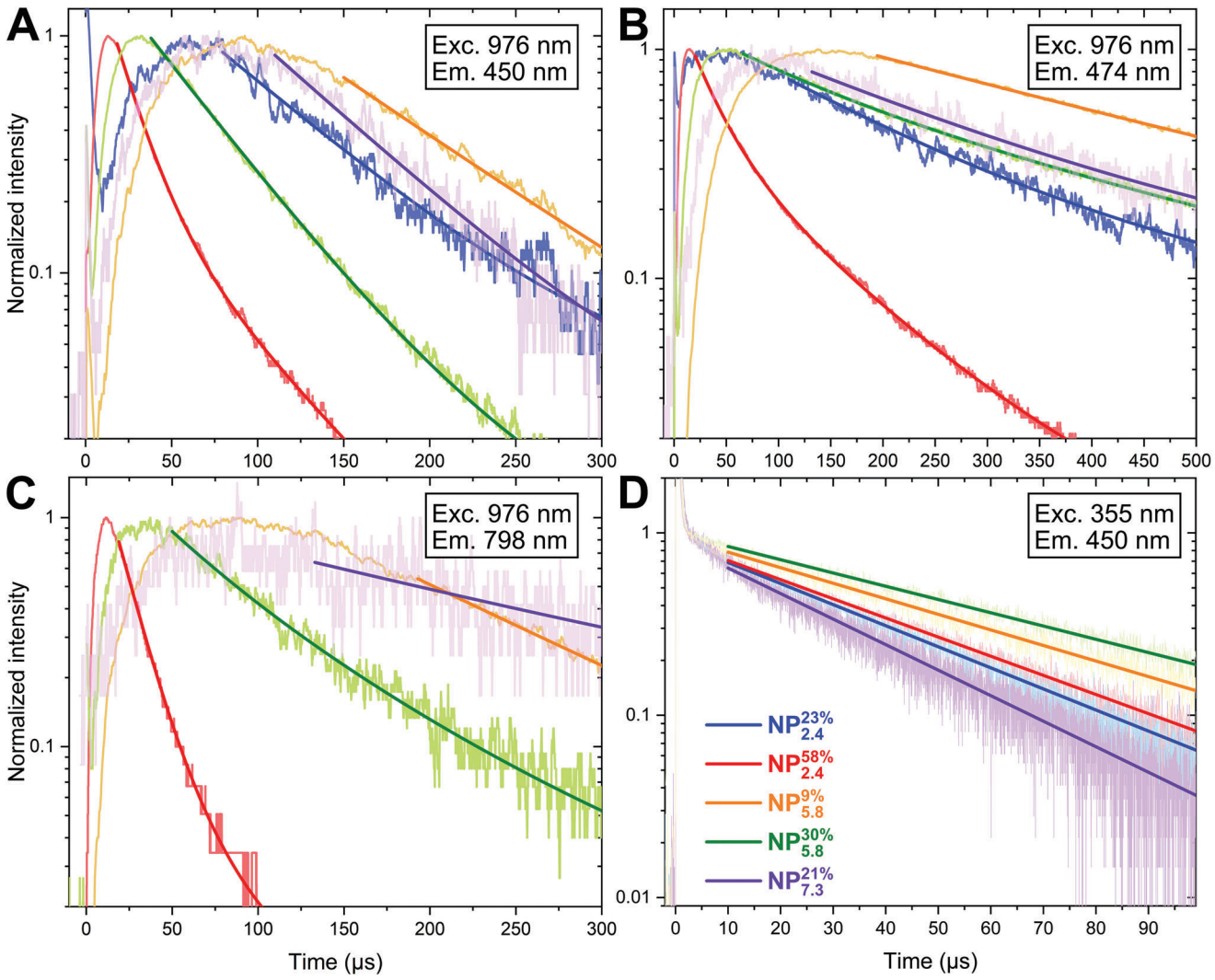

Figure 7. Time-resolved emissions at 450 474 and 798 nm with nanosecond laser excitation at 976 nm A–C respectively) and emission at 450 nm after a 355 nm nanosecond pulse D). The bold line is the respective results for the biexponential fit (A–C, see Figure S7, Supporting Information) and monoexponential fit D). The first short decay observed in panel D is due to laser scattering.

to 20% leads to an increase in the contribution of the emission arising from $^1G_4$ as seen for single-Tm^{3+} $NP^{58\%}_{2.8}$ and $NP^{23\%}_{2.4}$ core particles which differ mostly in Yb concentration. This can be assigned to faster Yb energy migration resulting in stronger surface quenching of excited Yb and less ETU. In the case of CS particles ($NP^{30\%}_{5.8}$ and $NP^{9\%}_{5.8}$) this effect is observed to a larger extent giving rise to a very strong contribution of the 474 nm band in $NP^{9\%}_{5.8}$ compared to $NP^{30\%}_{5.8}$. The stronger contribution of the 474 nm band in CS particles compared to their core counterparts may indicate that the surface quenching process is efficiently reduced increasing the probability of ETU and the population of excited Tm^{3+} ions.[13,43,66–69]

These observations were rationalized using time-resolved spectroscopy upon nanosecond single pulse excitation (**Figure 7**) which can provide more detailed information on the dynamics of the $^1D_2$ (4 ETU 450 nm) $^1G_4$ (3 ETU 474 nm) and $^3H_4$ (2 ETU 798 nm) states. Using such short pulses only one Tm^{3+} ion per nanoparticle is expected to be excited which should therefore limit the contribution of CR processes to only CR4. After excitation at 976 nm two regimes are observed: (i) a rise of the signal due to building of the state through ETU until the disappearance of excited Yb^{3+} and (ii) a multiexponential decay illustrating the complex ETU dynamics SQ and CR between the different Tm^{3+} states and the relaxation toward the ground state.

According to the series of measured lifetimes gathered in **Table 2** under NIR excitation (976 nm) both $\langle\tau\rangle_{a450}$ ($^1D_2$) and $\langle\tau\rangle_{a474}$ ($^1G_4$) decrease with increasing %Yb ($NP^{58\%}_{2.8}$ versus $NP^{23\%}_{2.4}$ and $NP^{30\%}_{5.8}$ versus $NP^{9\%}_{5.8}$). $NP^{58\%}_{2.8}$ core NPs lacking shell protection and possessing a high Yb proportion display the shortest lifetime under NIR irradiation. As previously mentioned for CW irradiation increasing the Yb^{3+} content in the core results in faster energy migration from the core to the surface through the sensitizer lattice and induces an increase in surface quenching. In agreement with stationary emission CS-type particles show increased luminescence decay time constants compared to the core

Table 2. Amplitude-averaged luminescence decay times (in µs) of the five UCNPs under study. The nonradiative decay rate k_{nr} (Equation 3) was estimated using the decay times measured in this work and the radiative decay time reported in Villanueva-Delgado et al. for a 0.01% Tm^{3+} β-$NaYF_4$ glass.[70] (* $\langle\tau\rangle_{a798}$ could not be accurately determined for C_1^{20} because of the very poor experimental signal-to-noise ratio).

	Exc. @ 976 nm			Exc. @ 355 nm	$k_{nr} \times 10^{-3}$ s^{-1}
	$\langle\tau\rangle_{a450}$ [µs]	$\langle\tau\rangle_{a474}$ [µs]	$\langle\tau\rangle_{a798}$ [µs]	τ_{450} [µs]	
$NP_{2.4}^{23\%}$	70.1 ± 0.3	261.4 ± 6.4	*	37.6 ± 0.1	11.80 ± 0.08
$NP_{2.8}^{58\%}$	24.5 ± 0.1	65.5 ± 1.5	18.2 ± 0.3	41.4 ± 0.1	9.36 ± 0.10
$NP_{5.8}^{9\%}$	101.4 ± 1.0	400.3 ± 2.4	131.5 ± 1.3	50.9 ± 0.3	4.83 ± 0.12
$NP_{5.8}^{30\%}$	49.9 ± 0.3	287.3 ± 1.0	74.9 ± 2.9	59.7 ± 0.2	1.94 ± 0.08
$NP_{7.3}^{21\%}$	66.3 ± 0.3	309.3 ± 26.0	220.3 ± 3.5	31.0 ± 0.1	17.43 ± 0.12

particles independent of their Yb^{3+} content ($NP_{2.4}^{23\%}$ versus $NP_{5.8}^{9\%}$ and $NP_{2.8}^{58\%}$ versus $NP_{5.8}^{30\%}$).

In addition the relaxation of the $^1D_2$ state of Tm after 355 nm UV irradiation is expected to be a good descriptor to analyze the competition between the different energy transfer processes because the sensitizer is bypassed (no ETU no EM). An advantage of such experiments is that while upconversion excitation is characterized by a growing and multiexponential decay the emission dynamics of the $^1D_2$ state upon 355 nm nanosecond excitation are characterized by a monoexponential decay (Figure 7D). Time constants are provided in Table 2. From the simplified Diecke diagram (**Figure 8A**)[70,71] a kinetic equation for the decay of the population of the $^1D_2$ state can be derived neglecting Tm^{3+}-to-Yb^{3+} back energy transfer (this assumption is justified as the increase in the Yb concentration does not imply a decrease in the $^1D_2$ lifetime under UV irradiation Table 2):

$$\frac{dN_4}{dt} = -\left(k_{4r} + k_{4SQ} + \omega_{CR4}N_0\right) N_4 \text{ with } \tau = \frac{1}{k_{4r}+k_{4SQ}+\omega_{CR4}N_0} \quad (2)$$

where N_0 is the number of Tm^{3+} ions in the $^3H_6$ ground state and N_4 is the number of Tm^{3+} ions in the $^1D_2$ excited state. k_{4r} is the global first-order depopulation rate constant of the $^1D_2$ state including the radiative processes and the nonradiative relaxation except for surface quenching and cross relaxation. k_{4SQ} is the nonradiative depopulation rate due to surface quenching and ω_{CR4} represents the CR4 energy transfer coefficient between two Tm^{3+} ions (Figure 8A).

For the core particles $NP_{2.4}^{23\%}$ and $NP_{2.8}^{58\%}$ the decay time constant τ_{450} is slightly shorter for $NP_{2.4}^{23\%}$ (τ_{450} = 37.6 µs) than for $NP_{2.8}^{58\%}$ (τ_{450} = 41.4 µs) while both nanoparticles contain a similar number of Tm^{3+} ions per particle. Considering that CR4 has a low probability in both particles that contain less than 2 Tm^{3+} ions/NP this result is thus assigned to the larger size of $NP_{2.8}^{58\%}$. $NP_{2.8}^{58\%}$ has a surface-to-volume ratio of 2.1 nm^{-1} where surface quenching is slightly less severe than in $NP_{2.4}^{23\%}$ with a surface-to-volume ratio of 2.6 nm^{-1}. As k_{4r} represents the decay rate of the $^1D_2$ state in the absence of CR and surface quenching its value can be approximated to the known $^1D_2$ decay time measured for a 0.01% Tm^{3+} β-$NaYF_4$ glass at 450 nm (k_{4r} = 14.8 10^3 s^{-1}).[70] This allows to separate the contributions of surface quenching and cross relaxation from the experimental rate constant of the

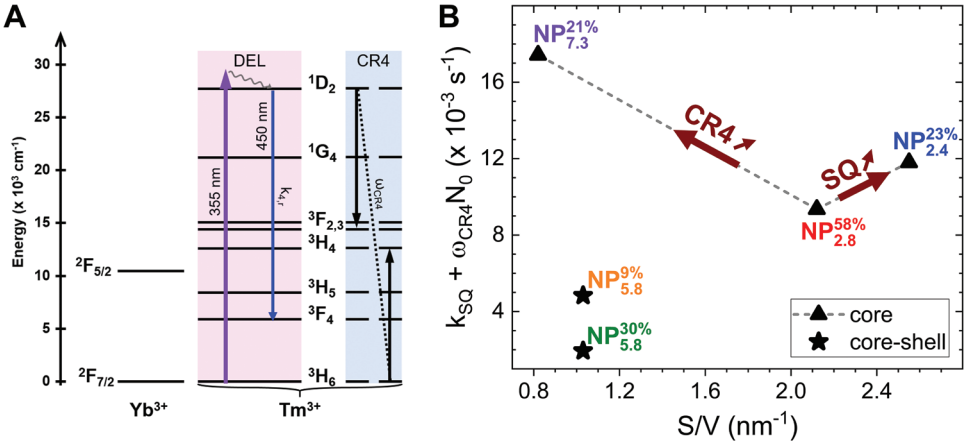

Figure 8. A) Energy level diagram of Na(Gd-Yb)F_4:Tm^{3+} UCNPs highlighting the transitions explored with 355 nm (Tm^{3+} direct excitation DE) light and the CR4 cross relaxation process. Solid straight arrows represent photon absorption and emission and the dotted line symbolizes the CR energy transfer. B) Estimated nonradiative rate constants (sum of the surface quenching and CR4 rate constants) of core (triangles) and core-shell (stars) particles plotted as a function of the surface-to-volume ratio.

global processes. These contributions are thus defined as follows (Table 2, Figure 8B):

$$k_{4nr} = k_{4SQ} + \omega_{CR4}\, N_0 = \frac{1}{\tau} - 14.8\ 10^3 \quad (3)$$

In particular the lifetime measured for the core particles for which CR4 is unlikely enables an estimation of the surface quenching rate constant of 11.80 10^3 s^{-1} for particles with an average diameter of 2.4 nm and of 9.36 10^3 s^{-1} for 2.8 nm average diameter particles. The respective contributions of CR and surface quenching are estimated by comparing the 450 nm time-resolved emission of the 20% Yb^{3+} 7.3 nm core particle $NP_{7.3}^{21\%}$ with that of its ultrasmall counterparts $NP_{2.4}^{23\%}$ and $NP_{2.8}^{58\%}$. Despite a lower surface-to-volume ratio (Figure 8B) the lifetime of the large particle is shorter (31.0 µs versus ≈ 40 µs) and the calculated k_{4nr} value is found to be the largest of the 5 considered UCNPs (17.43 10^3 s^{-1} Table 2 and Figure 8B). This illustrates the importance of CR4 in the non-radiative deactivation of the 450 nm Tm^{3+} emission.

For the core-shell particles the lifetimes obtained by direct UV excitation were always longer for the CS particles than for the parent core particles revealing the lowest k_{4nr} values of 4.83 10^3 s^{-1} and 1.94 10^3 s^{-1} for $NP_{5.8}^{9\%}$ and $NP_{5.8}^{30\%}$ respectively. As the number of Tm^{3+} ions/NP is similar in these two particles with the same average diameter the different nonradiative rate constants can only be explained by a different structure. $NP_{5.8}^{30\%}$ is more likely a core-shell nanoparticle with a fairly effective protective layer whereas for $NP_{5.8}^{9\%}$ intermixing of the core and shell probably occurs reducing the protective effect of the shell and explaining the difference in lifetime. A possible reason for this difference is that the smaller $NP_{2.4}^{23\%}$ particle giving the $NP_{5.8}^{9\%}$ particle in the core-shell architecture is predicted to be twice as soluble as the $NP_{2.8}^{58\%}$ particle (used to prepare $NP_{5.8}^{30\%}$) because of its smaller size making its respective CS counterpart different in terms of the core-shell architecture.

3. Conclusion and Outlook

We have proposed a new method to prepare hexagonal highly monodisperse ultrasmall UCNPs containing only 1 Tm^{3+} ion/NP using a synthesis involving temperature cycling adapted to the thermal microwave-assisted coprecipitation route. Starting from our original approach involving a gadolinium-rich formulation in situ mixing of the precursors NaOH and NH_4F and high-power microwave heating we have shown that replacing the high-temperature plateau by a temperature cycling sequence enabled precise control of the particle size dispersity. Emission decay lifetime analysis was found to provide a relevant descriptor of the completion of the α-to-β phase transition. Although the average particle size reveals more variability nanoparticles below 3 nm in diameter containing one Tm^{3+} activator ion on average could be synthesized using such a protocol. The reduced amount of active components i.e. Yb^{3+} and Tm^{3+} ions allows these particles to bridge the gap between standard UCNPs and upconversion molecular complexes. Despite their very small size and limited number of activators the crystals are still luminescent under 980 nm excitation. Shielding procedure of these very small UCNPs with an inert $NaGdF_4$ shell led to brighter nanoparticles with a size of 5.8 nm. These particles could not be described as simple core-shell architectures because of larger size and larger number of activators per particle than expected. Analysis of the luminescence lifetimes after UV nanosecond pulse excitation revealed that a protection do occur because the non radiative rate constants are clearly lower than in the core UCNPs however to a different extent in the two CS particles. This is attributed to different intermixing between core and shell material.

Decreasing the size of UCNPs down to less than 3 nm inevitably brings strong quenching effects coming from the high surface-to-volume ratios but simultaneously reduces the likelihood for activator concentration quenching induced by cross relaxation as the number of Tm^{3+} ions per UCNP is also automatically reduced. In single-emitter nanoparticles comparison of NIR excitation and direct UV excitation shows that the upconversion dynamics for ultrasmall UCNPs is controlled by energy migration of Yb^{3+} ions and their surface quenching. Direct excitation of Tm^{3+} ions allows to evaluate their surface quenching rate constant. In addition we show that cross relaxation is responsible for the massive quenching of the 450 nm emission in larger particles (7.3 nm). In 1% Tm^{3+} UCNPs this quenching due to cross relaxation becomes more important than the surface quenching occurring in the ultrasmall particles (2.4 and 2.8 nm). Thus the number of excited and nonexcited Tm^{3+} ions is a crucial factor to be considered when studying ultrasmall UCNPs. Poisson statistics show that while the average number of Tm^{3+} ions per nanoparticle is ≈1 40% of particles have 2 or more Tm^{3+} ions. The next step is thus a study of the lifetime versus excitation power at the single-particle level. Our results emphasize that by combining fine tuning of the number of activators per particle via an optimized synthesis pathway and an appropriate excitation scheme (CW NIR ns pulse UV ns pulse) it is possible to select the operating CR processes and to provide an accurate analysis of the different mechanisms at play in these model nanoparticles.

4. Experimental Section

Synthesis: $RECl_3.xH_2O$ NH_4F technical grade oleic acid (OA) and 1-octadecene (ODE) were purchased from Alfa Aesar and used as received. All other organic solvents were of spectroscopic grade and used as received. Deionized water (ρ = 18 MΩ cm^{-1}) was obtained from an Aquadem apparatus. Microwave heating was performed using a monomode Monowave 300 oven from Anton-Paar Company. Conventional heating steps were performed in 100 mL three-neck round-bottom flasks heated by a high-power heating mantle from Horst Company placing the temperature probe directly in contact with the reaction mixture.

Monitoring of the Microwave-Assisted High-Temperature Cycling Procedure—RE Oleates: A 2 mL solution of $RECl_3.xH_2O$ (42% Gd 57%Yb 1% Tm) in deionized water was added to a mixture of OA:ODE (60 mL and 150 mL for 2 mmol RE) in a 500 mL three-necked flask and water was carefully distilled off. The cloudy mixture was then brought to 160 °C under a gentle argon flush until no solid material remained. The pale-yellow clear solution was then cooled under an argon atmosphere and used without further analysis.

In Situ Mixing: According to the previously published protocol[51,65] two methanol solutions of NaOH (1 g 25 mmol 80 mL) and NH_4F (1.48 g 40 mmol 80 mL) were simultaneously added with the help of two syringe pumps to a vigorously stirred solution of the above-prepared metal oleate over 1h30 (0.2–0.4 mL min^{-1}) to reach a final 1:2.5:4 RE:Na:F ratio. Methanol was gently evaporated before carefully degassing the resulting mixture at 100 °C.

The *reaction mixture* was transferred via 4 mL aliquots into Ar-flushed MW reactors and then heated in the MW oven as discussed in the results

section. For each sample x cycles (x = 1 to 6) were applied: 1) heating as fast as possible up to 300 °C, 2) holding at a temperature plateau of 300 °C for 1 min, 3) cooling to 280 °C (in 2 s), and 4) holding at a temperature plateau of 280 °C for 5 min.

Particles were then isolated by precipitation in an EtOH solution of combined crude mixtures followed by centrifugation at 9000 g for 10 minutes. After redispersion in cyclohexane the particles were washed twice by precipitation in EtOH and centrifuged again. They were finally dispersed and stored in cyclohexane.

Synthesis of Ultrasmall Core (Sub-3 nm) and Core-Shell Na(Gd-Yb)F_4:Tm^{3+}: The preparation of ultrasmall core (sub-3 nm) Na(Gd-Yb)F_4:Tm^{3+} followed the above-described procedure 5-fold downscaled. The MW heating step was performed by applying 5 heating cycles.

Each suspension of ultrasmall cores was divided into 2 equal portions (1 mmol RE per portion) with one being stored and the other being used for the synthesis of the corresponding core@shell. For this purpose 1 mmol Gd$(OA)_3$ was prepared in a 1:1 mixture of OA:ODE (20 mL:20 mL) as described above. After cooling to room temperature this Gd$(OA)_3$ solution and 5 mmol CF_3COONa in 4 mL of MeOH dissolved in 10 mL of cyclohexane were added to the suspension of core NPs so that the final proportions were n(RE)core = n(Gd)shell = 1 mmol. Cyclohexane and MeOH were then removed at 100 °C. After careful degassing the mixture was transferred via 15 mL aliquots into argon-flushed MW reactors and then heated up in the MW as fast as possible (54 °C min^{-1}) to 300 °C for 15 min. Particle purification was achieved as described above (precipitation centrifugation dispersion centrifugation and redispersion).

Synthesis of 7.5 nm Na(Gd-Yb)F_4:Tm^{3+} UCNPs: A similar reaction mixture to that for ultrasmall cores was prepared (1.2 mmol RE: 79%Gd 20%Yb 1% Tm in OA:ODE (12 mL:30 mL)). After methanol removal and thorough degassing at 100 °C the resulting mixture was directly heated using a conventional heating mantle up to 280 °C (20 °C min^{-1}) and then maintained at this temperature for 90 min. Particle purification was achieved as mentioned above.

Analyses and Characterization—Powder X-ray Diffraction: (XRD) measurements of the dried samples were performed on a Bruker D8 Advance diffractometer working with monochromatized Cu Kα1 radiation (λ = 1.5406 Å). The photon energy detection window of the fast LynxEye detector was set to avoid the RE fluorescence signal. Disoriented single-crystalline silicon sample holders were used to lower their contribution to the background line. The patterns were collected in the 10–90° 2θ angular range with a step size of 0.05 °.

Transmission Electron Microscopy: (TEM) was performed on a Hitachi HT-7700. TEM images were analyzed with ImageJ by using the free PSA (Particle Size Analyzer version r12) macro. Size distributions were then fitted by a Gaussian function with OriginLab for ease of visualization with the size and standard deviation (1 σ) being given for several thousands of measurements for each sample.

Inductively Coupled Plasma Optical Emission Spectrometry: (ICP-OES) was used to determine the UCNP relative composition in terms of the elements Gd Yb and Tm (icap 7000 THERMO SCIENTIFIC). Samples were prepared by digestion of the particles in nitric acid.

Steady-State Luminescence: Spectra were measured using a commercial fluorimeter (Fluoromax-3 Horiba Jobin Yvon) equipped with a fiber-Bragg-grating 976 nm polarized stabilized laser diode (Thorlabs 900 mW) with temperature stabilization (Arroyo 6340 ComboSource controller). The beam was focused into a 4×10 mm quartz cuvette (with the 4 mm dimension along the laser propagation direction) without stirring of the solution by a convergent lens (focal length of 50.2 mm) providing a Gaussian intensity distribution in the plane perpendicular to light propagation direction at the focal point of 88 µm ($1/e^2$). The power density at the sample was 6.85 kW cm^{-2} (Ophir NOVA II + PD300-1 W). The emission was collected at 90° (10 mm cuvette thickness) versus 976 nm light and the slit of the simple monochromator was set to a 5 nm bandpass. The emission spectra were recorded between 300 and 850 nm with a 1 nm step. Emission spectra were corrected for the wavelength dependence of the detector spectral sensitivity using the correction function provided by the instrument manufacturer. An additional correction was carried out by subtracting the solvent signal (cyclohexane).

To monitor the influence of the number of temperature cycles steady-state luminescence measurements at 798 nm were acquired with a standard PTI QuantaMaster 400 fluorimeter equipped with a fiber continuous wave (CW) 980 nm multimode laser (MDL-H 980 nm Acal BFi/Changchun Industry) at 35.4 W cm^{-2} (Figure 2B). The beam was collimated before passing through the cuvette.

Time-Resolved Luminescence: Measurements were performed using two different irradiation schemes and setups: (i) millisecond square pulses (976 nm) and (ii) nanosecond pulses (976 nm and 355 nm).

(i) Millisecond Square Irradiation was used to examine the synthesized particles obtained with different microwave heating sequences (1 to 6 cycles). This irradiation was achieved using an LDH laser head at 976 nm operating in the CW mode with a Taiko PDL M1 controller (Picoquant) and a fast gate input (rise time of a few µs, see Figure S3, Supporting Information) using a delay generator (SRS model DG535) as the source signal allowing the generation of square millisecond pulses of variable duration. The experiments were performed with 3 ms square pulses at a frequency of 200 Hz *i.e.* the UCNPs were irradiated every 5 ms by a 3 ms square pulse at 976 nm. The choice of the pulse length was guided by the time necessary to reach the photostationary state with the fluence used. The laser beam was focused into a 4 × 10 mm quartz cell (with the 10 mm dimension along the laser direction) placed in the chamber of a fluorescence lifetime spectrometer in which the solutions were stirred (FluoTime200 Picoquant). The emitted photons were collected at 90° through a monochromator (bandpass of 16 nm) and detected by an MCP-PMT detector (Hamamatsu). The arrival time of the photons was measured using a photon counting card working in multichannel scaling mode in long-range mode (TimeHarp260pico). The laser power density was estimated to be 100 W cm^{-2} at the sample i.e. ca. 0.13 mJ per pulse. The time resolution was set at 1.6 µs.

(ii) Nanosecond Pulse Irradiation was employed to reveal the dynamics of the Tm^{3+} emission in the optimized UCNPs as a function of the number of Tm^{3+} ions the concentration of Yb^{3+} ions and the effect of a surface shielding shell. The experiments were performed using a laser flash photolysis apparatus.[72] Two different ns pulses were used to irradiate the UCNPs either to probe the Tm^{3+} upconversion process by exciting the Yb^{3+} sensitizer (976 nm) or to directly probe the Tm^{3+} $^1D_2$ excited state (355 nm). The energies used in these experiments reached 2 mJ $pulse^{-1}$ at 976 nm and 2.5 mJ $pulse^{-1}$ at 355 nm. The beam diameter at the focal point was estimated to be 70 µm (FWHM of the Gaussian fit). Samples were stirred in a quartz cell (4 × 10 mm with the 4 mm dimension along the nanosecond laser direction). To study the upconversion process nanosecond polarized pulses at 976 nm (FWHM of 7–8 ns 1 mJ 2 Hz) were provided by a 10 Hz Nd:YAG laser (Continuum Surelite II) coupled to an OPO (Continuum Panther EX OPO) and an SH05 shutter (Thorlabs). UCNPs were irradiated by 8 ns pulses every 0.5 s. The emitted light was collected at 90° versus the ns pulse dispersed by a monochromator (Horiba Jobin-Yvon iHR320 bandpass of 10 nm grating of 600 frames mm^{-1}) and collected by a photomultiplier (R1477-06 Hamamatsu) coupled to a high voltage supply set at 1 kV. The signal from the PMT was measured by a digital oscilloscope (LeCroy 454 500 MHz entrance impedance of 1 MΩ coupled to a resistance of 4.7 kΩ). The instrument response function (IRF) was then determined to be about 2 µs (decay of the laser scattering signal). Emission dynamics were measured at 4 wavelengths (360 450 474 and 798 nm) for 1 to 5 milliseconds (10 000 points resolution 100 to 500 ns) and each recorded trace was an average of 64 experiments. On the other hand Tm^{3+} direct excitation was carried out using the 355 nm light resulting from the tripled Nd:YAG laser emission (same laser and detection described above). Here the emitted light at 450 nm was collected and no resistance was used for the detection of the PMT signal. In this case the IRF had a decay time of 200 ns based on the laser scattering signal.

Supporting Information

Supporting Information is available from the Wiley Online Library or from the author.

Acknowledgements

B.A. and A.E. equally contributed to this work. The authors acknowledge CNRS and the Agence Nationale de la Recherche (Grant ANR-15-CE09-0020 BLINK) for financial support. B.A., C.R., J-C.M., and C.C. acknowledge the Université Paul Sabatier for financial support the CMEAB platform for TEM support and N. Ratel-Ramond (CEMES) for XRD support. B.A. acknowledges the German Academic Exchange Service (DAAD) for financial support (Short-Term Grant No. 91709165). A.E., A.B., and M.S. acknowledge the Université de Lille and Région Hauts de France for financial support. M.P. and F.G. acknowledge the Université de Rennes for financial support. F.G. acknowledges B. Lefeuvre for ICP measurements and Dr. G. Loas and A. Carré for technical support. The authors would like to thank Prof. M. Haase (Univ. Osnabrück) for fruitful discussions.

Conflict of Interest

The authors declare no conflict of interest.

Data Availability Statement

The data that support the findings of this study are available from the corresponding author upon reasonable request.

Keywords

cross relaxation, single-emitter particles, surface quenching rate constant, temperature cycling, ultrasmall upconversion nanoparticles

Received: April 30, 2024
Revised: May 22, 2024
Published online:

[1] F. Auzel, *Chem. Rev.* **2004**, *104*, 139.
[2] J.-C. G. Bünzli, S. V. Eliseeva in *Lanthanide Luminescence*,(Eds: P. Hänninen, H. Härmä), Series on Fluorescence, Springer, Berlin Heidelberg **2011**, pp 1–45.
[3] S. Wilhelm, *ACS Nano* **2017**, *11*, 10644.
[4] H. Dong, L.-D. Sun, C.-H. Yan, *Chem. Soc. Rev.* **2015**, *44*, 1608.
[5] P. A. Tanner, L. Zhou, C. Duan, K.-L. Wong, *Chem. Soc. Rev.* **2018**, *47*, 5234.
[6] A. Teitelboim, B. Tian, D. J. Garfield, A. Fernandez-Bravo, A. C. Gotlin, P. J. Schuck, B. E. Cohen, E. M. Chan, *J. Phys. Chem. C* **2019**, *123*, 2678.
[7] Y. Wu, M. J. Y. Ang, M. Sun, B. Huang, X. Liu, *J. Phys. D: Appl. Phys.* **2019**, *52*, 383002.
[8] K. Malhotra, D. Hrovat, B. Kumar, G. Qu, J. V. Houten, R. Ahmed, P. A. E. Piunno, P. T. Gunning, U. J. Krull, *ACS Appl. Mater. Interfaces* **2023**, *15*, 2499.
[9] E. M. Mettenbrink, W. Yang, S. Wilhelm, *Adv. Photon. Res.* **2022**, *3*, 2200098.
[10] K. Zarschler, L. Rocks, N. Licciardello, L. Boselli, E. Polo, K. P. Garcia, L. De Cola, H. Stephan, K. A. Dawson, *Nanomed.: Nanotechnol. Biol. Med.* **2016**, *12*, 1663.
[11] B. H. Kim, M. J. Hackett, J. Park, T. Hyeon, *Chem. Mater.* **2014**, *26*, 59.
[12] K. Huang, H. Ma, J. Liu, S. Huo, A. Kumar, T. Wei, X. Zhang, S. Jin, Y. Gan, P. C. Wang, S. He, X. Zhang, X.-J. Liang, *ACS Nano* **2012**, *6*, 4483.
[13] R. Shi, C. D. S. Brites, L. D. Carlos, *Small Struct.* **2022**, *3*, 2100194.
[14] D. J. Gargas, E. M. Chan, A. D. Ostrowski, S. Aloni, M. V. P. Altoe, E. S. Barnard, B. Sanii, J. J. Urban, D. J. Milliron, B. E. Cohen, P. J. Schuck, *Nat. Nanotechnol.* **2014**, *9*, 300.
[15] J. Zhao, Z. Lu, Y. Yin, C. McRae, J. A. Piper, J. M. Dawes, D. Jin, E. M. Goldys, *Nanoscale* **2013**, *5*, 944.
[16] B. Golesorkhi, A. Fürstenberg, H. Nozary, C. Piguet, *Chem. Sci.* **2019**, *10*, 6876.
[17] R. C. Knighton, L. K. Soro, A. Lecointre, G. Pilet, A. Fateeva, L. Pontille, L. Francés-Soriano, N. Hildebrandt, L. J. Charbonnière, *Chem. Commun.* **2021**, *57*, 53.
[18] A. M. Nonat, L. J. Charbonnière, *Coord. Chem. Rev.* **2020**, *409*, 213192.
[19] L. J. Charbonnière, *Dalton Trans.* **2018**, *47*, 8566.
[20] B. Golesorkhi, S. Naseri, L. Guénée, I. Taarit, F. Alves, H. Nozary, C. Piguet, *J. Am. Chem. Soc.* **2021**, *143*, 15326.
[21] H. Fu, C. Hu, J. Liu, Q. Zhang, J. Y. Xu, G. J. Jiang, M. Liu, *CrystEngComm* **2022**, *24*, 7698.
[22] M.-H. Du, D.-H. Wang, L.-W. Wu, L.-P. Jiang, J.-P. Li, L.-S. Long, L.-S. Zheng, X.-J. Kong, *Angew. Chem., Int. Ed.* **2022**, *61*, 202200537.
[23] N.-F. Li, X.-M. Luo, J. Wang, J.-L. Wang, H. Mei, Y. Song, Y. Xu, *Sci. China: Chem.* **2022**, *65*, 1577.
[24] F. Wang, R. Deng, X. Liu, *Nat. Protoc.* **2014**, *9*, 1634.
[25] G. Chen, H. Qiu, R. Fan, S. Hao, S. Tan, C. Yang, G. Han, *J. Mater. Chem.* **2012**, *22*, 20190.
[26] A. D. Ostrowski, E. M. Chan, D. J. Gargas, E. M. Katz, G. Han, P. J. Schuck, D. J. Milliron, B. E. Cohen, *ACS Nano* **2012**, *6*, 2686.
[27] Y. Zhang, Z. Yu, J. Li, Y. Ao, J. Xue, Z. Zeng, X. Yang, T. T. Y. Tan, *ACS Nano* **2017**, *11*, 2846.
[28] C. Li, L. Xu, Z. Liu, Z. Li, Z. Quan, A. A. Kheraif, J. Lin, *Dalton Trans.* **2018**, *47*, 8538.
[29] T. Joshi, C. Mamat, H. Stephan, *ChemistryOpen* **2020**, *9*, 703.
[30] F. Huang, L. Labrador-Páez, H. Ågren, L. Wang, J. Zhang, R. Pu, Q. Zhan, J. Widengren, H. Liu, *Nano Energy* **2023**, *105*, 108015.
[31] J. Chen, L. Liang, S. Tan, S. Xi, C.-H. Lin, T. Wu, Q. He, X. Liu, *Nano Lett.* **2023**, *23*, 7221.
[32] D. A. Gálico, E. M. Rodrigues, I. Halimi, J. Toivola, H. Zhao, J. Xu, J. O. Moilanen, X. Liu, E. Hemmer, M. Murugesu, *Nat. Commun.* **2024**, *15*, 3498.
[33] M. D. Wisser, S. Fischer, P. C. Maurer, N. D. Bronstein, S. Chu, A. P. Alivisatos, A. Salleo, J. A. Dionne, *ACS Photonics* **2016**, *3*, 1523.
[34] F. Wang, X. Liu, *Chem. Soc. Rev.* **2009**, *38*, 976.
[35] R. Naccache, Q. Yu, J. A. Capobianco, *Adv. Opt. Mater.* **2015**, *3*, 482.
[36] R. Shi, A.-V. Mudring, *ACS Mater. Lett.* **2022**, *4*, 1882.
[37] T. Sugimoto, *Adv. Colloid Interface Sci.* **1987**, *28*, 65.
[38] Y. Yin, A. P. Alivisatos, *Nature* **2005**, *437*, 664.
[39] B. Voss, M. Haase, *ACS Nano* **2013**, *7*, 11242.
[40] R. Arppe, I. Hyppanen, N. Perala, R. Peltomaa, M. Kaiser, C. Wurth, S. Christ, U. Resch-Genger, M. Schaferling, T. Soukka, *Nanoscale* **2015**, *7*, 11746.
[41] C. Siefe, R. D. Mehlenbacher, C. S. Peng, Y. Zhang, S. Fischer, A. Lay, C. A. McLellan, A. P. Alivisatos, S. Chu, J. A. Dionne, *J. Am. Chem. Soc.* **2019**, *141*, 16997.
[42] M. Y. Hossan, A. Hor, Q. Luu, S. J. Smith, P. S. May, M. T. Berry, *J. Phys. Chem. C* **2017**, *121*, 16592.
[43] C. Würth, S. Fischer, B. Grauel, A. P. Alivisatos, U. Resch-Genger, *J. Am. Chem. Soc.* **2018**, *140*, 4922.
[44] Y. Wang, *Nanoscale* **2019**, *11*, 10852.
[45] Z. Wu, S. Yang, W. Wu, *CrystEngComm* **2016**, *18*, 2222.
[46] R. Kacker, M. Radoiu, H. J. M. Kramer, *Cryst. Growth Des.* **2017**, *17*, 3766.
[47] R. Kacker, P. M. Salvador, G. S. J. Sturm, G. D. Stefanidis, R. Lakerveld, Z. K. Nagy, H. J. M. Kramer, *Cryst. Growth Des.* **2016**, *16*, 440.
[48] Z. Wu, S. Seok, D. H. Kim, W.-S. Kim, *Cryst. Growth Des.* **2015**, *15*, 5675.
[49] P. N. Vakil, D. A. Hardy, G. F. Strouse, *ACS Nano* **2018**, *12*, 6784.
[50] D. Li, W.-Y. Lai, Q. Shao, W. Huang, *Inorg. Chem. Front.* **2017**, *4*, 1211.
[51] B. Amouroux, C. Roux, J.-D. Marty, M. Pasturel, A. Bouchet, M. Sliwa, O. Leroux, F. Gauffre, C. Coudret, *Inorg. Chem.* **2019**, *58*, 5082.

[52] C. Dong, J. Pichaandi, T. Regier, F. C. J. M. van Veggel, *J. Phys. Chem. C* **2011**, *115*, 15950.
[53] J. A. Damasco, G. Chen, W. Shao, H. Ågren, H. Huang, W. Song, J. F. Lovell, P. N. Prasad, *ACS Appl. Mater. Interfaces* **2014**, *6*, 13884.
[54] J. Liu, G. Chen, S. Hao, C. Yang, *Nanoscale* **2017**, *9*, 91.
[55] X. Liu, L. Yan, S. Liu, Q. Li, B. Zhou, *Optik* **2020**, *207*, 164398.
[56] J. Czerny, F. Heil, C. J. Egbers, M. Haase, *Chem. Mater.* **2020**, *32*, 5691.
[57] A. Alizadehkhaledi, A. L. Frencken, F. C. J. M. van Veggel, R. Gordon, *Nano Lett.* **2020**, *20*, 1018.
[58] A. M. Kotulska, A. Pilch-Wróbel, S. Lahtinen, T. Soukka, A. Bednarkiewicz, *Light: Sci. Appl.* **2022**, *11*, 256.
[59] G. Tessitore, A.-V. Mudring, K. W. Krämer, *New J. Chem.* **2018**, *42*, 237.
[60] S. Radunz, A. Schavkan, S. Wahl, C. Würth, H. R. Tschiche, M. Krumrey, U. Resch-Genger, *J. Phys. Chem. C* **2018**, *122*, 28958.
[61] G. Wang, W. Qin, J. Zhang, L. Wang, G. Wei, P. Zhu, R. Kim, *J. Alloys Compd.* **2009**, *475*, 452.
[62] T. van Westen, R. D. Groot, *Cryst. Growth Des.* **2018**, *18*, 4952.
[63] J. D. Suter, N. J. Pekas, M. T. Berry, P. S. May, *J. Phys. Chem. C* **2014**, *118*, 13238.
[64] E. Andresen, F. Islam, C. Prinz, P. Gehrmann, K. Licha, J. Roik, S. Recknagel, U. Resch-Genger, *Sci. Rep.* **2023**, *13*, 2288.
[65] X. Zhai, Y. Wang, X. Liu, S. Liu, P. Lei, S. Yao, S. Song, L. Zhou, J. Feng, H. Zhang, *ChemPhotoChem* **2017**, *1*, 369.
[66] T. Sun, R. Ma, X. Qiao, X. Fan, F. Wang, *ChemPhysChem* **2016**, *17*, 766.
[67] C. Homann, L. Krukewitt, F. Frenzel, B. Grauel, C. Würth, U. Resch-Genger, M. Haase, *Angew. Chem., Int. Ed.* **2018**, *57*, 8765.
[68] N. J. J. Johnson, S. He, S. Diao, E. M. Chan, H. Dai, A. Almutairi, *J. Am. Chem. Soc.* **2017**, *139*, 3275.
[69] F. T. Rabouw, P. T. Prins, P. Villanueva-Delgado, M. Castelijns, R. G. Geitenbeek, A. Meijerink, *ACS Nano* **2018**, *12*, 4812.
[70] P. Villanueva-Delgado, K. W. Krämer, R. Valiente, M. de Jong, A. Meijerink, *Phys. Chem. Chem. Phys.* **2016**, *18*, 27396.
[71] S. L. Maurizio, G. Tessitore, K. W. Krämer, J. A. Capobianco, *ACS Appl. Nano Mater.* **2021**, *4*, 5301.
[72] Y. Pellegrin, M. Sandroni, E. Blart, A. Planchat, M. Evain, N. C. Bera, M. Kayanuma, M. Sliwa, M. Rebarz, O. Poizat, C. Daniel, F. Odobel, *Inorg. Chem.* **2011**, *50*, 11309.